Investigation of isothermal oxidation performance of TiAl alloys sintered by different processing methods

Yiğit Garip

Sakarya Applied Science University, Technology Faculty, Department of Metallurgy and Materials Engineering, Esentepe Campus, 54187, Sakarya, Turkey

ARTICLE INFO

ABSTRACT

The production of TiAl alloys can be a discouraging task owing to their low ductility at room temperature. However, the development of novel methods that are alternative to traditional methods for producing TiAl alloys is a fundamental aspect for structural applications in the automotive and aerospace industries. Resistance sintering method enables the production of TiAl alloys, thanks to a combination of remarkable attributes such as shorter sintering time, fast heating rates. This method is promising under circumstances where the rapid densification, short sintering time and low cost becomes a great advantage. The objective of the following work was to compare the isothermal oxidation performance of TiAl alloys produced by resistance sintering (RS) and pressureless sintering (PS) methods. After oxidation at 900 °C for 200 h, the final weight change of RSed alloy ($6.36 \, \text{mg/cm}^2$) was lower than that of PSed alloy ($8.92 \, \text{mg/cm}^2$). X-ray diffraction (XRD), scanning electron microscopy (SEM), and energy-dispersive spectroscopy (EDS) were performed to characterize the oxidized alloys. Analyses results show that the oxidation products were TiO_2 and Al_2O_3 oxides, the oxide scale of both alloys are composed a multilayered structure. The relatively continuous Al_2O_3 layer formed on the scale of RSed alloy played a major role in enhancing the oxidation resistance of the alloy.

1. Introduction

Great demands on the production of materials with remarkable properties for high-temperature structural applications have triggered the development of cost-effective, eco-friendly and more productive non-conventional processing routes. However, powder metallurgy processing route has a combination of attractive features, such as preparation of material with superior mechanical properties, controllability, faster preparation process, a material with good dimensional stability, economic advantage, ease of reproducibility, lesser human contact and minimum inherent defects [1,2]. Resistance sintering (RS) technology is one of the non-traditional sintering techniques in the field of powder metallurgy that allows the production of bulk materials with higher density from elemental powders utilizing rapid heating rates lower external pressure and shorter processing times at lower temperatures compared to conventional sintering techniques [3,4]. RS technique, which enables the densification of powders in one-step characterized by the simultaneous application of a high-intensity current, low-voltage and uniaxial pressure, is a cost-effective and eco-friendly method for the production of TiAl alloys. The high intense electric current flowing through the powder mass or compact placed inside a die induces

generation of heat by the Joule effect. In addition, due to the fast heating and cooling rates during operation, the grain growth can be controlled, resulting in a microstructure with fine-grained and high-density [5,6]. Another important advantage of the RS technique is the elimination of post-production operations, which adds a considerable cost in manufacturing. Moreover, economic benefits are also provided because of low energy consumption and material wastage. Compared to conventional techniques, RS technology shortens processing time from a few hours to minutes, thereby achieving the productivity growth that is important for engineering applications.

Among the intermetallic compounds, the outstanding properties of alloys based on titanium aluminides have made them a demanded material in high-temperature structural applications such as aerospace, automotive and gas turbine industries. These alloys possess superior attributes, including high melting point, low density, adequate high specific strength, creep resistance and elastic modulus as well as good oxidation and corrosion resistance [7–10]. Numerous investigations have been conducted to enhance the oxidation resistance of TiAl alloys, most of which were related to the effect of alloying elements of ternary or quaternary. It has been stated that the oxidation resistance of TiAl alloys was increased by the addition of Mo, W, Nb and Si [11,12].

Knowledge of the effect of electric current on the oxidation behavior of the TiAl alloys is of crucial importance for developing non-conventional processing routes to produce these alloys. This work aims to investigate the isothermal high temperature oxidation resistance of at.% Ti–44Al–2Si-1.7Mn-0.3W alloys produced via different processing routes: resistance sintering (RS) and pressureless sintering (PS). In accordance with this aim, sintered microstructure, oxidation kinetics, scale structure, and oxidation mechanism were explored. However, this work would pave the way for comparing oxidation behaviors of TiAl alloys produced by different processing methods.

2. Experimental procedure

2.1. Process of the powder preparation and sintering

The TiAl alloys used in the present work had the nominal composition of Ti–44Al–2Si-1.7Mn-0.3W (in atomic percent). The elemental powders were composed of Ti (40 μm, 99.5% purity), Al (7–15 μm, 99.5% purity), Si (5 μm, 99.9% purity) Mn (10 μm, 99.6% purity) and W (4 μm 99.9% purity). The powders were weighed by an electronic balance of high accuracy of 0.01 mg in accordance with the nominal

composition and poured into a plastic container with stainless steel grinding balls. Afterward, a mechanical mixer was used to achieve a homogenous powder mixture for a duration of 5 h at a speed of 200 rpm in a dry environment. The ball-to-powder weight ratio (BPR) used during the milling process was 5:1. For both resistance sintering (RS) and pressureless sintering (PS) experiments, the blended powder compositions were poured into separate steel dies with an inner diameter of 20 mm. However, before the powder mixture is poured, the internal wall of the die and the punches in contact with the powder mixture were used the high-temperature lubricant spray to help remove the product after sintering and also reduces the friction of the components in contact with the die wall during the sintering. For the RS experiment, the powder mass in the die to be sintered is placed between two counter-sliding punches. After that, the RS system was activated with optimized process parameters: electric current of 4.5 kA, dwell time of 15 min at a uniaxial pressure of 80 MPa and in air atmosphere. The used current was optimized to be the same as the temperature in the PS experiments. At the completion of sintering, the electric current was stopped, the uniaxial pressure was released, and the sintered sample was allowed to cool to ambient temperature.

For the PS experiment, the powders were first pressed by a uniaxial
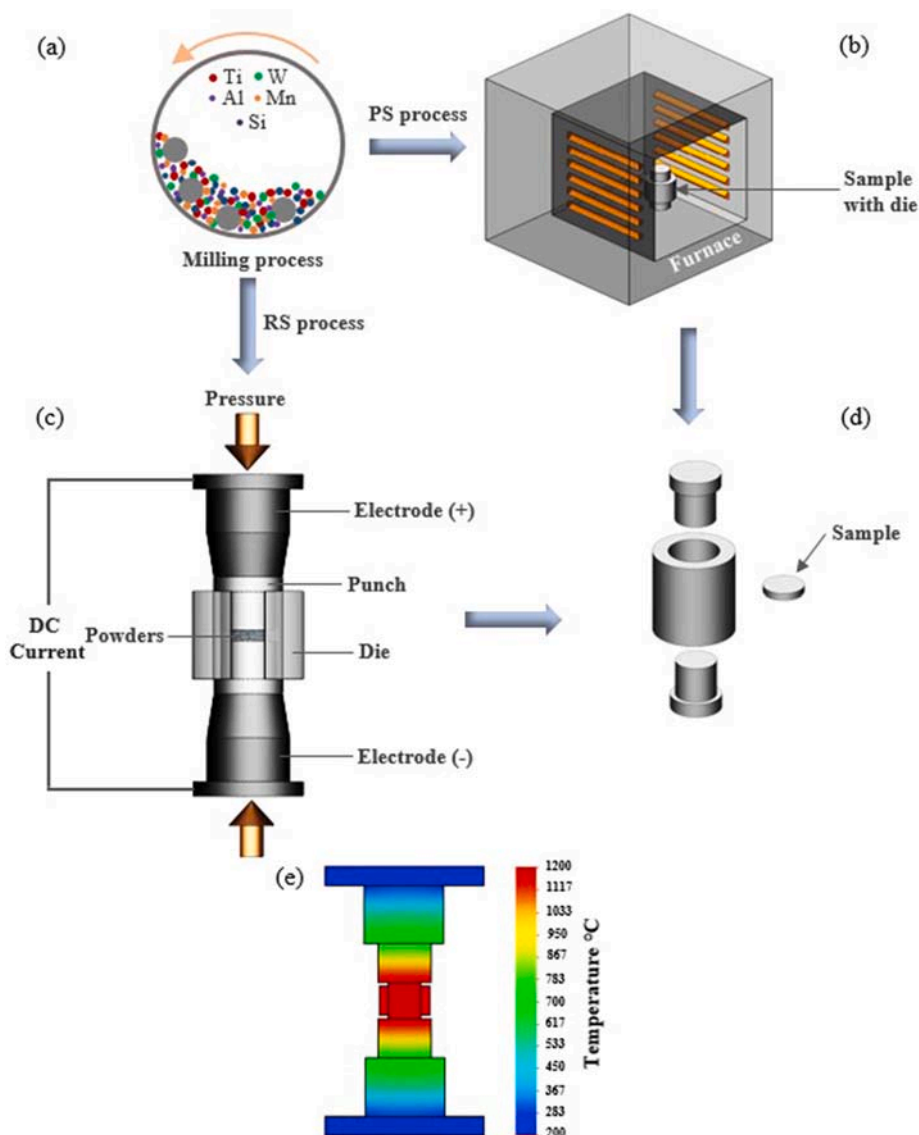

Fig. 1. Schematic of the experimental procedure used in the work, (a) ball milling, (b) PS process, (c) RS apparatus, (d) die components and sample, and (e) generation of thermal gradient during RS modeled by Solidworks software.

under 80 MPa in a steel die to obtain compact. After that, the compact was placed in a muffle furnace in order to sintering. The PS experiment was conducted with a heating rate of 20 °C/min up to the sintering temperature of 1050 °C, at a dwelling time of 120 min and in air atmosphere. When the experiment was complete, the resistance heating was turned off. The schematic diagrams of the RS and PS systems are presented in Fig. 1.

2.2. Isothermal oxidation experiment

Isothermal oxidation tests were conducted in a muffle furnace at 900 °C for 200 h. The samples were placed in a separate alumina crucible and transferred to the furnace for the purpose of being oxidized. Weight change measurements were performed at intervals of oxidation for 5, 10, 25, 50, 100, 150 and 200 h by using a digital balance with an accuracy of 0.01 mg in order to evaluate the oxidation kinetics. To continue the experiment, the samples with the crucibles were put into the furnace to re-oxidized.

In order to carry out the metallographic examinations, both samples before and after oxidation were gradually grounded by SiC papers up to 1200 and subsequently polished using 1 μm diamond particles. After that, the samples were etched by a Kroll's reagent: 3 vol % HF, 5 vol % HNO_3, 92 vol % distilled water. X-ray diffraction analysis (Rigaku, D/MAX-B/2200/PC) was used to identify the phase constitution of the samples and oxidation products using diffractometer with Cu Kα radiation and operated at 20 kV. The XRD data scanning angle 2θ ranges from 20° to 90° with a step size of 0.02°. The initial microstructures of the samples, the surface morphology and the cross-sectional microstructure of the oxidized samples were inspected by a scanning electron microscopy (SEM, JEOL JSM-6060, LV). Chemical compositions of the present phases were analyzed by energy-dispersive spectroscopy (EDS, IXRF 5000).

The densities of the sintered samples were calculated by Archimedes' principle, based on the immersion technique in distilled water. The microhardness measurements of the samples were performed using a Vickers Hardness tester with a diamond indenter. The microhardness measurements were conducted at different regions under a 500 g load for a duration of 10 s. The microhardness value of both samples was determined according to the arithmetic mean of four different measurements. Meanwhile, the samples produced by RS and PS will hereafter denote as RSed and PSed, respectively.

3. Results and discussion

3.1. Microstructure evolution

XRD analysis results in Fig. 2 show that the microstructure of both alloys was composed of $α_2$-Ti_3Al (hexagonal structure) and γ-TiAl (face-centered tetragonal structure) phases. Among the intermetallic phases existed in the binary TiAl system, $α_2$-Ti_3Al and γ-TiAl phases are reported to be important for engineering applications [13]. However, dual

Fig. 2. XRD patterns of the RSed and PSed alloys.

phase ($α_2$+γ) based TiAl alloys have attracted the attention of researchers for many years due to their satisfactory properties [14]. As shown in Fig. 2, the microstructure of both alloys produced using RS and PS techniques consists of dual phase. According to the binary TiAl phase diagram, TiAl alloy with the composition of at.% 44 Al solidifies from the single-phase region of the α during the cooling as follows: α → α+γ → $α_2$+γ. Considering the mechanism of phase transformation for products formed, during sintering, when the temperature of the powder mixture reaches the melting temperature of Al, liquid Al reacts with Ti to form the $TiAl_3$ phase; Ti + 3Al = $TiAl_3$. Furthermore, maximum solubility of Ti in Al is about at.% 0.1 at 600 °C, while that of Al in Ti is at.%12 [15]. This allows us to conclude that the nucleation of $TiAl_3$ phase starts. From the thermodynamic point of view, the Gibbs free energy of formation of $TiAl_3$ is the lowest compared to those of other intermetallic compounds (Table 1).

As the sintering progresses with time, TiAl and Ti_3Al are formed by the reaction of resultant $TiAl_3$ and remnant Ti, and this continues till the $TiAl_3$ is consumed [17]; 4Ti + $TiAl_3$ = 2TiAl + Ti_3Al.

Anselmi-Tamburini et al. [18] studied the effect of the current on the growth kinetics of the product phase in the Mo–Si system and they reported the current played a significant role in enhancing the growth rate of the product phase, however, the values of formation activation energy of this phase in case of the current and current free were the same. According to these authors, the applied electric current did not change the reaction mechanism. Studies involving comparison of densification kinetics of the powders by SPS and HP indicated that the electric current has no remarkable effect on the densification mechanism [19,20]. However, as mentioned in the experimental part of this work, the sintering times of RSed and PSed alloys were 15 min and 120 min, respectively. An important point to be emphasized is what effect the causes shortening of sintering time. The role of current on the improved densification during RS sintering can be attributed to mass transport. Mass transport may induce a change in defect concentration [18], electromigration [20], and a reduction in the activation for migration of the defects [21]. This can contribute to the driving force for the enhanced densification and phase transformation. As more specific, the effect of the current on mass transport can be explained form the electromigration theory [22]:

$$J_i = -\frac{D_i\,C_i}{RT}\left[\frac{RT\,\partial\,In\,C_i}{\partial x} + F\,z^*\,E\right] \tag{1}$$

where J_i denotes the atomic flux, D_i denotes the diffusivity, C_i denotes the atomic concentration, R denotes the gas constant, T denotes the temperature, F denotes the Faraday's constant, z^* denotes the effective charge on the diffusing species, and E denotes the field.

Based on Eq. (1), the applied electric field provokes a deviation in the random walking behavior of diffusion species. In return, the driving force of sintering for PS technique is provided from the surface curvature of the powder particles, but this is inadequate to annihilate the pores at the last sintering stage [23].

The SEM micrographs of RSed and PSed alloys and the chemical compositions corresponding to the points are shown in Fig. 3. It can be seen that the SEM micrograph of both alloys mainly exhibits a similar microstructure with gray contrast phase and dark-gray contrast phase. By considering the EDS analysis in combination with the XRD results, the gray contrast phase (points 1 and 5) was found to be an $α_2$-Ti_3Al and the dark-gray phase (points 2 and 6) was found to be a γ-TiAl.

Table 1
Temperature dependence of Gibbs free energy for TiAl intermetallic compounds [16].

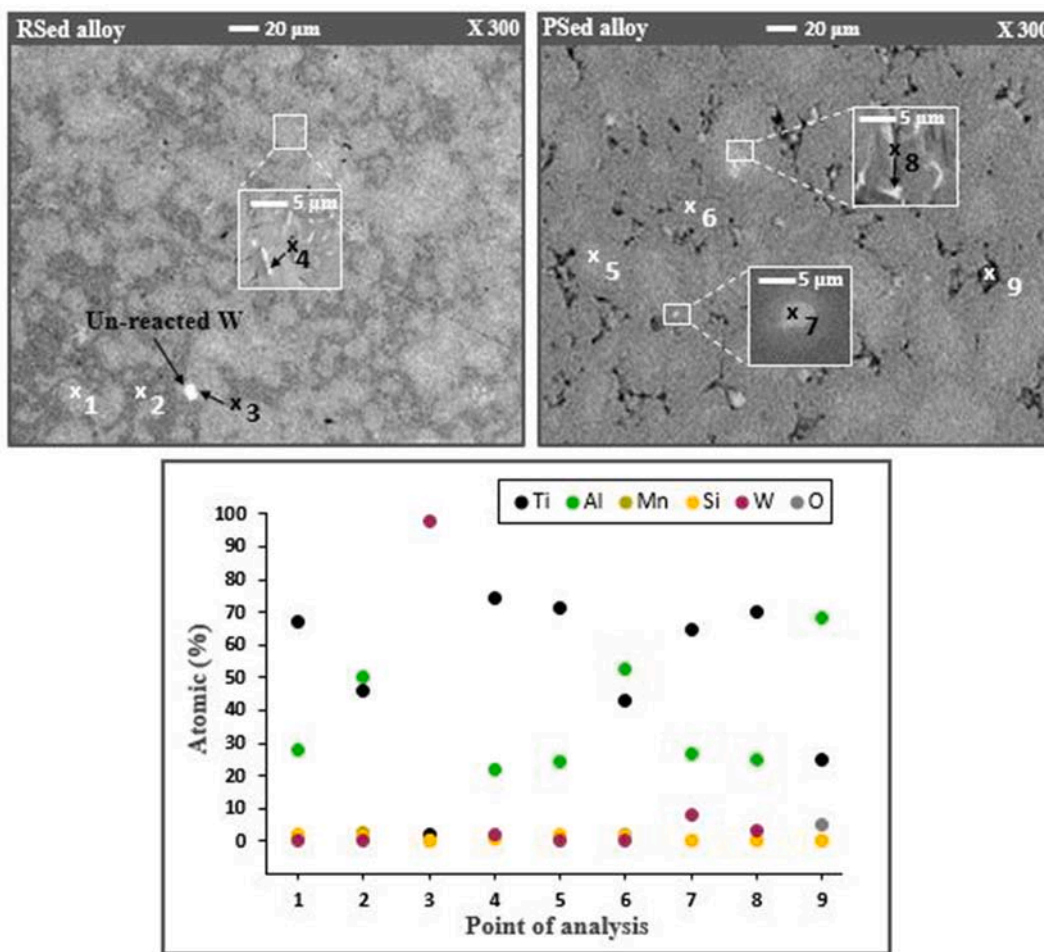| Compounds	Gibbs free energy
Ti_3Al	−29,633.6 + 6.70801T
TiAl	−37,445.1 + 16.7937T
$TiAl_3$	−40,349.6 + 10.36525T
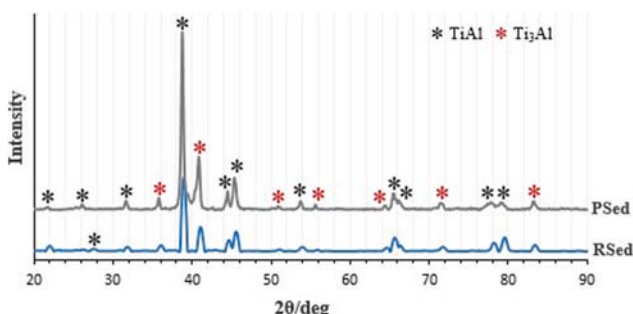
Fig. 3. SEM micrographs of the microstructure of RSed and PSed alloys and corresponding EDS analysis results.
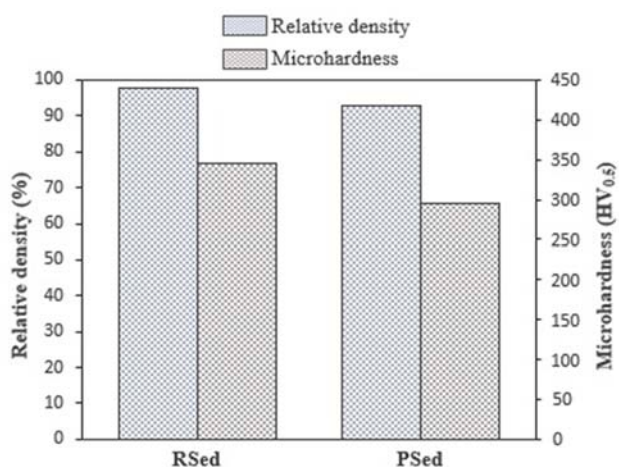

Fig. 4. Comparison of the relative density and microhardness results of RSed and PSed alloys.

Additionally, the un-reacted W (point 3) can be seen on the surface of the RSed alloy. However, a magnified view of the marked area showed that the W-rich phases in bright contrast (point 4) were also present in the microstructure. The EDS analysis of point 4 indicates that W is reacted with other constituent elements, which means that the diffusion of W particles has occurred (except point 3). As for the microstructure of PSed alloy, the chemical composition of point 7 showed the W was

partially diffused and its content was about at.% 7.5. According to the EDS results shown in Fig. 3, the chemical composition of point 8 which lies on the bright phase was grossly similar to that of point 4. Moreover, the SEM micrograph of PSed alloy highlighted that the free W particles were absent in the microstructure. It is worthwhile noting that Ti, Al, Mn, and Si elements were homogeneously distributed in the whole alloys. This indicated that the production conditions used in this work in both methods were enough for the diffusion of these elements; however, the diffusion of W was more restricted under these conditions. A primary challenge associated with manufacturing of W-containing alloys is due to the high melting point of W element. Therefore, this leads to the W particles remain without diffusion within the alloy. However, the overall observation regarding the diffusion of W was one of the promising results achieved in this work. In comparison with the RSed alloy, the presence of a minor amount of oxygen was detected at point 9 on the PSed alloy. However, owing to the RS method shortening of processing time provided a remarkable advantage in reducing the oxygen uptake during sintering. It is of specific interest to note that the microstructure of PSed alloy contains a significant amount of porosity compared to that of the RSed alloy. In addition, Table 2 revealed that the relative density

Table 2
The densification and microhardness attributes of RSed and PSed alloys.

Alloy	Microhardness $(HV_{0.5})$	Experimental density (g cm^{-3})	Theoretical density (g cm^{-3})	Relative density (%)
RSed	349 ± 17	4.108	4.198	97.85
PSed	298 ± 13	3.876	4.198	92.32

of RSed alloy was 97.85% while that of the PSed alloy was 92.32%. The fact behind the enhanced densification in PSed alloy is that the applied pressure has a crucial role in particle re-arrangement and the annihilation of agglomerates [22]. Further to say, the combined effect of the high heating rate and the applied external pressure is believed to provide an increased driving force to enhance densification. In a study on the synthesis and densification of Ti–48Al–2Cr–2Nb, Lagos et al. [24] concluded that when the pressure was enhanced from 15 MPa to 50 MPa the maximum density was achieved at very low temperature (around 630–650 °C). The obtained microhardness values of both alloys are shown in Table 2 (see Fig. 4).

3.2. Weight change analysis

The isothermal oxidation resistance of RSed and PSed alloys was characterized by their weight change per unit area as a function of oxidation time. The weight change data of both alloys that were isothermally oxidized at 900 °C for 200 h are displayed in Fig. 5. The curves of weight change indicated that the oxidation rate of both alloys is increased with increasing time. However, as oxidation proceeded, the difference between the weight changes of alloys became more pronounced. Regardless of whether the processing is performed via RS or PS, one can be seen that the oxidation rate of alloys increases rapidly during the initial 25 h of oxidation. For instance, the weight change of RSed and PSed alloys was 2.75 and 4.60 mg/cm^2, respectively. In the first 25 h which fast oxidation process occurred, the formation of TiO$_2$ and Al$_2$O$_3$ is regarded to occur concurrently on the surface of alloys due to the fact that the Ti and Al elements have a high affinity for O at temperatures over 450 °C [25,26]. Moreover, the unoxidized surface is believed to promote nucleation and growth of oxides at the TiAl surface easily during the initial state oxidation. The above considerations caused a significant weight change to be recorded in both alloys. After the initial oxidation state, the unfavorable rate of the weight change per unit area decreased with progressing time. The mechanism behind this observed result can be evaluated based on the two aspects, the first is that the diffusion distance of reactive species through the scale and subjacent alloy increases owing to the increase in scale thickness. The second is that a rich Al$_2$O$_3$ layer, which prevents the inward diffusion of O, may have developed in the scale. The first consideration is related to the nature of parabolic oxidation kinetics, i.e. the weight change per unit area is high at initially but reduces with time. It could also be seen from Fig. 5 that the weight change of RSed alloy was smaller than that of PSed alloy during the experiment at 900 °C for 200 h. Comparison of the effect of processing route on the weight change of alloys shows that the final weight change of RSed alloy (6.36 mg/cm^2) is lower than that of PSed

alloy (8.92 mg/cm^2). It is important to mention that the spallation of oxide scale did not occur in both alloys during the oxidation experiment, indicating the strong adhesion of the oxide scale.

Analysis of the isothermal oxidation behavior of TiAl alloys with various composition in the existing literature can be contributed to compare the performance of our alloys. In a work conducted by Gong et al. [27] on the isothermal oxidation of the Ti–44Al–6Nb–1Cr–2V (at. %) alloy at 900 °C for 100 h, the alloy experienced a weight gain of about 8.6 mg/cm^2 after oxidized for 100 h. Pilone et al. [28] have studied the isothermal oxidation resistance of Ti–48Al–2Cr-1.5Nb-0.04B (at.%) alloy at 900 °C for 100 h, and their measurement results show that the final weight gain of the alloy was about 7 mg/cm^2. In a more recent work on the isothermal oxidation behavior of Ti-46.5Al–5Nb–2Cr-0.3B (at.%) alloy, Neelam et al. [29] found that the weight gain of the alloy reached 3.2 mg/cm^2 after oxidation at 900 °C for 500 h.

The knowledge of the mechanism that controls the growth of the oxide scale is crucial in understanding the oxidation behavior of alloys. In order to figure out what oxidation kinetics laws the weight change curves follow, a power-law equation can be used, $(\Delta W)^n = k_n t$, where ΔW is the specific weight change (mg/cm^2), n is the power exponent, k_n is the oxidation rate constant (mg^n/cm^{2n} h) and t is the oxidation time (h). In this regard, the values of power exponent (n) correspond to the slope of best fit line for a double logarithm plot of the weight change vs time. The power exponent is determined according to the n = 1/m, which is the reverse of the slope determined from the linear regression in Fig. 6a. The results obtained show that the n values for RSed and PSed alloys are 2.27 and 2.22, respectively. It is noted that the relationship between the n value and oxidation kinetics can be described as follows: n = 1, 2, 3 correspond to linear, parabolic and cubic kinetics, respectively. Accordingly, the oxidation behavior of investigated alloys obeys a nearly parabolic kinetic pattern where the power exponent (n) is close to 2, which indicates that the oxidation process in the alloys is diffusion-driven during the oxidation experiment for 200 h.

The results obtained from Fig. 6b showed that the oxidation rate constants (k_n) were 0.3586 and 0.6391 mg^n cm^{-2n} h^{-1} for the RSed and the PSed alloys, respectively. As it is well known, the oxidation resistance increases with decreasing the oxidation rate constant. This allows us to conclude that the oxidation behavior of RSed alloy was better than that of PSed alloy, under oxidation conditions used in the present work. It is also evident from the weight change plots corresponding to the oxidized alloys that RSed alloy enhanced oxidation resistance. That is to say, these kn values were in good agreement with the kinetic curve results.

3.3. Characterization of oxide scale

3.3.1. Phase compositions

Figs. 7 and 8 show the XRD patterns for oxidized alloys at 900 °C for 100 h and 200 h, respectively. At both duration of oxidation time, (Rutile) TiO$_2$, (Corundum) α-Al$_2$O$_3$ and TiAl phases are present in the XRD patterns. After 100 h of oxidation, the TiAl is the major phase for the RSed alloy, while the TiO$_2$ phase is the major phase for the PSed alloy. This difference in the XRD analysis of both alloys can be ascribed to the thickness of the oxide scale, thus diffraction signals can be detected from the substrate depending on the thickness of the scale. On the other hand, it could be observed that the diffraction peaks of TiO$_2$ were more intensity compared to that of Al$_2$O$_3$. This is because the Al$_2$O$_3$ layer cannot form on the outmost surface of alloy because of kinetic factors. These kinetic factors will be addressed in the oxidation mechanism of alloys. However, the oxides of Mn, Si and W were not detected as they may be dissolved in the scale. The XRD patterns in Fig. 7 indicate that increasing the exposure time from 100 to 200 h causes an increase in the TiO$_2$ intensity. However, weak diffraction signals corresponding to the TiAl were also observed in the XRD results. The XRD results highlighted that the increased exposure time plays an important role in
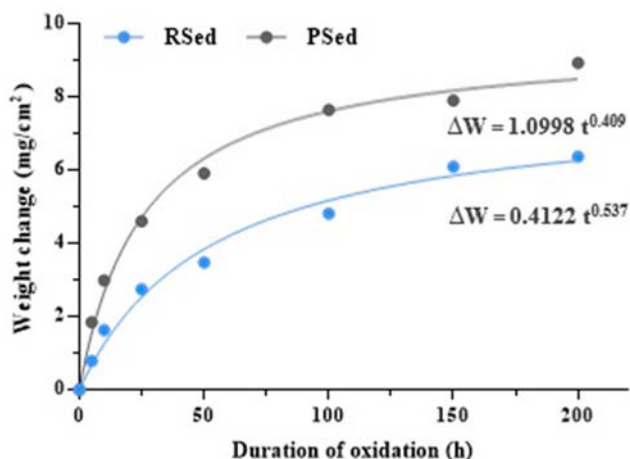
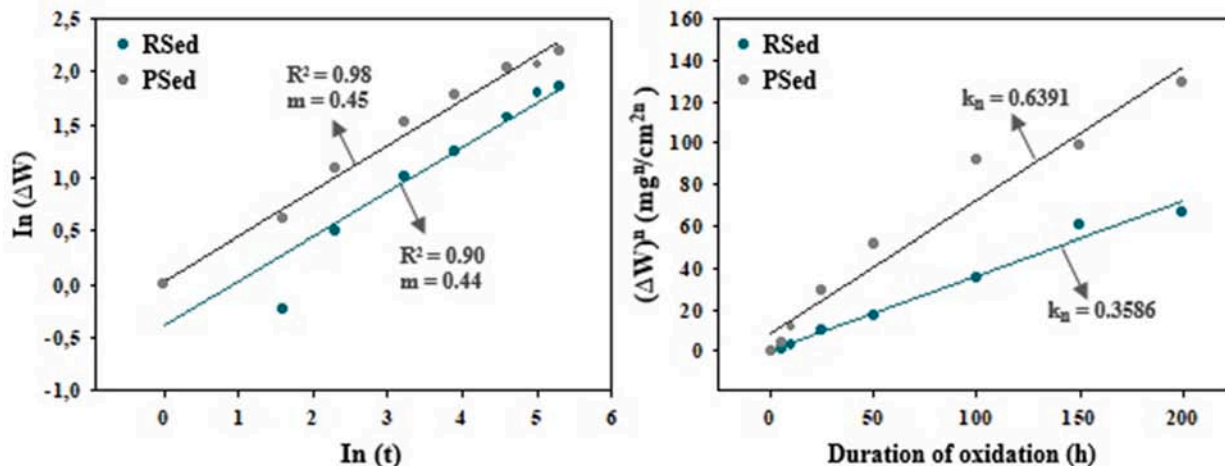**Fig. 5.** Weight change plot of the RSed and PSed alloys during isothermal oxidation at 900 for 200 h.

Fig. 6. Linearization plots of a) double logarithmic scales for ΔW versus t, b) ΔWⁿ versus t, in which the slopes of the lines fitted to the data indicate the rate constant for oxidized alloys.
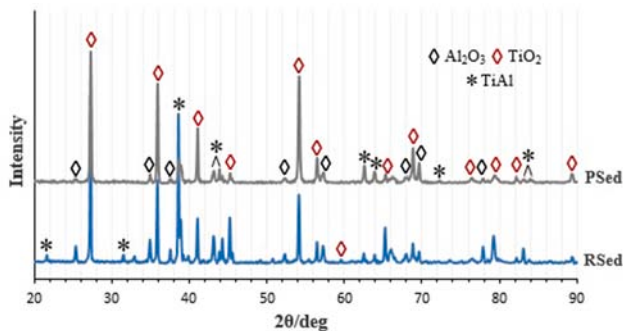

Fig. 7. XRD patterns of RSed and PSed alloys after oxidation at 900 °C for 100 h.
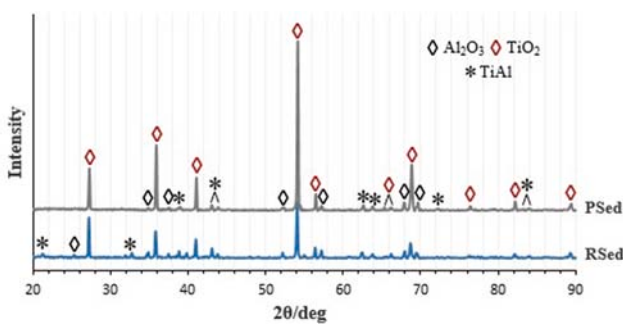

Fig. 8. XRD patterns of RSed and PSed alloys after oxidation at 900 °C for 200 h.

the growth of oxide scale. In a nutshell, the oxide scale of RSed and PSed alloys are composed of TiO_2, Al_2O_3 after oxidation at 900 °C for 200 h. The obtained results are in good agreement with the reports in the Refs. [30,31].

3.3.2. Surface morphology

Top surface morphologies of the RSed and PSed alloys after oxidation at 900 °C for 100–200 h are shown in Fig. 9. Fig. 10 shows the corresponding chemical composition of the points analyzed by EDS. The first point concerning the surface morphology results can be the effect of exposure time on the growth of the oxide scale. As can be seen in Fig. 9, the size of oxide grains formed on the surface is increased with

increasing oxidation time. According to the results of EDS analysis, regardless of oxidation time, the scales formed on both alloys were mainly composed of O, Ti and Al. In the case of oxidized RSed alloy for 100–200 h, Fig. 9a and b shows that the scale formed on the alloy consists of a flat area with dark contrast (points 1 and 3) and the relatively larger grains with gray contrast (points 2 and 4). The regions marked as 1 and 3 reveal that the Ti, Al and O are present in higher amounts, which indicates the formation of the TiO_2 and Al_2O_3 mixed layer. Chemical analysis by EDS in Fig. 10 indicates that the oxide grains with gray contrast (points 2 and 4) have composition corresponding to the TiO_2. The formation of Al_2O_3 and TiO_2 on the alloy is also confirmed by the XRD patterns of the oxidized alloys in Figs. 7 and 8. After 200 h of oxidation, the formation of the TiO_2 grains becomes pronounced over the whole surface of RSed alloy. The outgrowth of TiO_2 grains shows the polyhedron faceted structure. As far as PSed alloy is concerned, it can be noticed that the surface morphology of the alloy after oxidation for 100 h is similar to that of the RSed alloy after oxidation for 200 h. Compared with PSed alloy, the smaller oxide grains formed on the surface of RSed alloy can be contributed to improving the spalling resistance of oxide scale. However, there was no symptom of spallation of both alloys in this work. Similarly, SEM micrograph of the surface shows in Fig. 9cd that the scale was made up of a region with dark contrast (point 5) and another region with gray contrast (points 6 and 7). By considering the EDS results in Fig. 10, the chemical composition of the dark region consists of the predominantly Ti, Al and O thereby indicating the possibility of formation of TiO_2 and Al_2O_3 mixed layer. At points 6 and 7 with the gray contrast, Ti and O are present in a higher amount, as indicated in EDS results. By considering the combination of the XRD and EDS results, the chemical composition of these regions corresponded to the TiO_2 phase. When the duration of oxidation reaches 200 h (Fig. 9d), the whole surface of PSed alloy is mostly covered by irregularly oriented larger oxide grains with polyhedron-shape.

In the light of the above considerations, it can be said that the growth process of the scale is not altered by the processing route fundamentally, but its growth velocity is retarded. A slower oxide growth on the RSed alloy can be attributed to the fact that the porosity level of the alloy (see Table 2) influences the diffusion processes in such a manner that cations and anions transport through the substrate/scale is reduced. On the other hand, the TiO_2 formed on the alloys is deleterious to the oxidation behavior due to the fact that it behaves as a shortcut to transport oxygen into the substrate, resulting in further oxidation [6].

Another important point to highlight is that some regions on both scales experience different oxidation behavior, resulting in bumpy surface morphology, as evidenced in Fig. 9a–c. The surface morphology changes occurring during oxidation can be induced by the oxygen
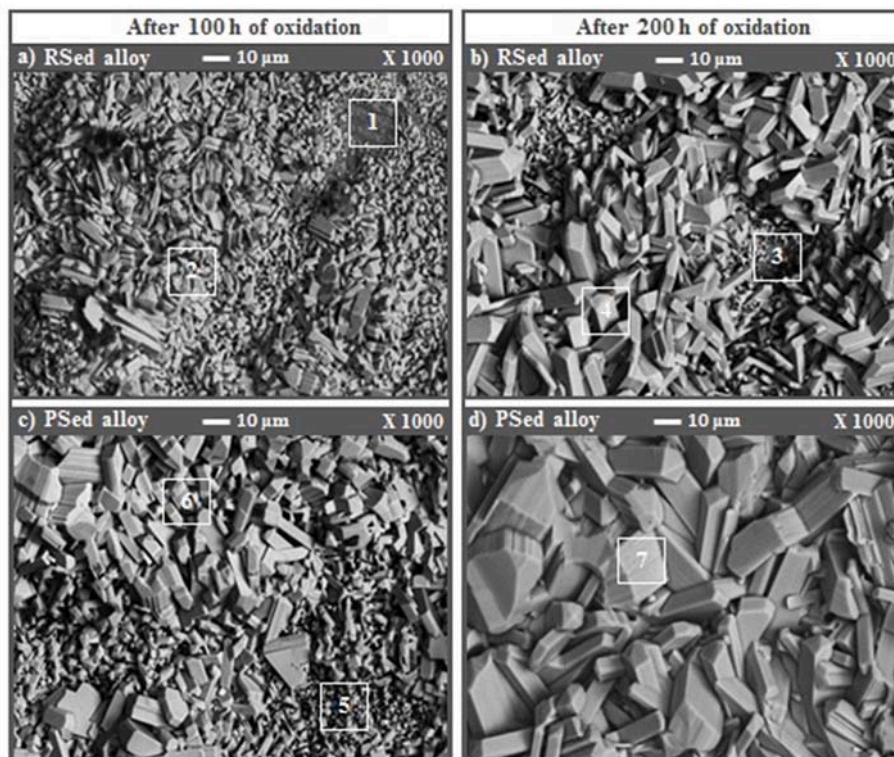
Fig. 9. Surface morphologies of the alloys after isothermal oxidation at 900 °C for (a)(c) 100 h and (b)(d) 200 h.
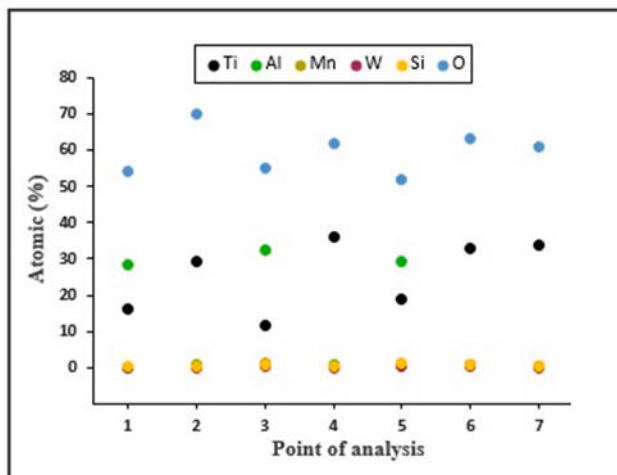
Fig. 10. Surface EDS point analysis of the after isothermal oxidation at 900 °C.

uptake. The presence of accelerated oxidation in these regions is an indication of the played role of oxygen uptake by the different phases. The fact behind this phenomenon is believed to be related to the different Ti and Al contents in these regions. That is to say, the regions, which contain the Ti_3Al phase, show that the Ti is present in a higher amount. The region with higher Ti activity increases the solubility of O, resulting in enhanced the formation of TiO_2. In the XPS study on oxidation of two-phased TiAl alloys at 650 °C, the dissolved oxygen content was measured to be 16 and 2 at.% in the phases of α_2 and γ-phases, respectively [32]. This allows us to conclude that the oxygen uptake for the α_2-phase is more critical due to its higher solubility compared to γ-phase. In line with the former cited work, in a more recent research done by Galetz et al. [33], it was characterized the oxidation-induced microstructural changes in Ti-43.5Al–4Nb–1Mo-0.1B

alloy at 900 °C, and they remarked that the dissolution of oxygen in α_2-phase was notable due to its vacancy structure. Besides, it should be mentioned that no sign of cracks can be seen from the surface of both alloys.

3.3.3. Cross-sectional morphology

Figs. 11 and 12 show the cross-section micrographs of the oxide scale formed on the RSed and PSed alloys after oxidation 900 °C for 200 h. EDS point analysis and elemental mapping analysis were conducted to examine the feature of the scale and the corresponding results are also available in Figs. 11 and 12. Combined with the cross-section micrographs and the elemental mapping analysis corresponding to the scale of alloys indicated that the oxide scales consisted of the multilayered structure. Each layer is made up of different phases; as shown in the BSE images, the outmost layer with a gray contrast, the intermediate layer with a dark contrast and the inner layer with mixture of gray and black contrast. The oxide scale of both alloys mainly contains Ti, Al and O as evidenced in EDS point analysis and elemental mapping analysis shown in Figs. 11 and 12. According to the combination of the corresponding EDS mapping and point analysis results (Fig. 11bc and 12bc, Ti and O are present in the high percentage at the outmost layers, which is marked with 1 (Figs. 11a and 12a), indicating the formation of TiO_2, as proved by XRD measurements shown in Fig. 8. The thickness of this layer is about 15 μm for RSed alloy, while it is about 21.5 μm for PSed alloy (Fig. 13). A thin dark contrast layer, which is marked with 2 on both scales, with a substantially higher concentration of Al and O is found beneath the TiO_2 layer. The chemical composition of these points corresponded to the Al_2O_3 phase, which is consistent with the XRD results. By considering the EDS mapping analysis, one can see that the intermediate layer is also composed of Al_2O_3. Moreover, beneath the TiO_2 the formed Al_2O_3 layer is more pronounced and keeps good bonding compared with that seen on PSed alloy. The area marked as 3 on both scales shows that the Ti, Al and O are present in higher contents, which indicates the oxides of Al and Ti coexisted in this layer. As can be noticed, this layer constitutes a substantial portion of the scale thickness;

Fig. 11. RSed alloy after oxidation at 900 °C for 200 h: a) cross-sectional micrograph, b) EDS point analysis and c) EDS elemental mapping analysis.

the average thickness of this layer was about 22 μm and 43 μm for RSed and PSed alloy (Fig. 13), respectively. Therefore, it can be recognized that the thickness of oxide scale formed on alloys was controlled by this TiO$_2$/Al$_2$O$_3$ mixed layer.

According to the results of oxide scale measurement, the overall thickness of the scale formed on RSed and PSed alloys was found to be 42.3 μm and 67.1 μm, respectively (Fig. 13). A thicker of the oxide scale on the PSed alloy provided evidence that the weight gain of PSed alloy is larger than that of RSed alloy, meaning that the PSed alloy has a higher oxidation rate. Besides, the oxide scales of both alloys showed good adherence to the substrate and the scale of both alloys was not cracked, indicating enhanced spallation resistance of the scale. Several pores are also seen in the outmost layer of both oxide scales. The inward diffusion of oxygen is rapid through the pores [27], indicating that the oxidation rate of alloys is increased. It is worthwhile noting that the additions of Si, Mn and W show a tendency to present more at the lower part of both scales because of their thermodynamic stability, as indicated in Figs. 11b and 12b.

Considering the above results, it is reasonable to conclude after 200 h of oxidation at 900 °C that the oxide scale structure of RSed and PSed alloys was not affected by the processing route, which results in the same oxide phases (namely TiO$_2$/Al$_2$O$_3$) and the similar scale morphology (multilayered). However, this work clarified the effects of processing

route on the oxidation behavior of the investigated alloys.

3.4. Oxidation mechanism of investigated alloys

The attribute of the oxide scale formed on the surface of alloys is crucial in providing the resistance of high-temperature oxidation. For this reason, investigation of the ability to form protective/continuous oxides film on the surface of all metallic materials at elevated temperatures is one of the most explored topics by many researchers.

Combined the results obtained in this work and literature data, the following oxidation mechanism can be proposed. In the first stage of oxidation, the dissolved O atoms adsorbed by TiAl surface cause the competition in the formation of TiO$_2$ and Al$_2$O$_3$ oxides because of the high affinity of Ti and Al to O, however, the reason for the preferential formation of TiO$_2$ is related to the preference of O atoms to Ti-rich regions [34]. As the oxidation continues, Ti and Al diffuse towards the surface to form their parent oxides. On the other hand, Gibbs free energy of formation of TiO$_2$ and Al$_2$O$_3$ are close in the Ellingham-Richardson diagram, which indicates that the nucleation and growth of both oxides occur simultaneously on the alloy surface. The results of the present work show that the oxide scale formed on RSed and PSed alloys consisted of TiO$_2$ and Al$_2$O$_3$ phases because the mentioned oxides are thermodynamically stable in the Ti–Al–O–N system when O is
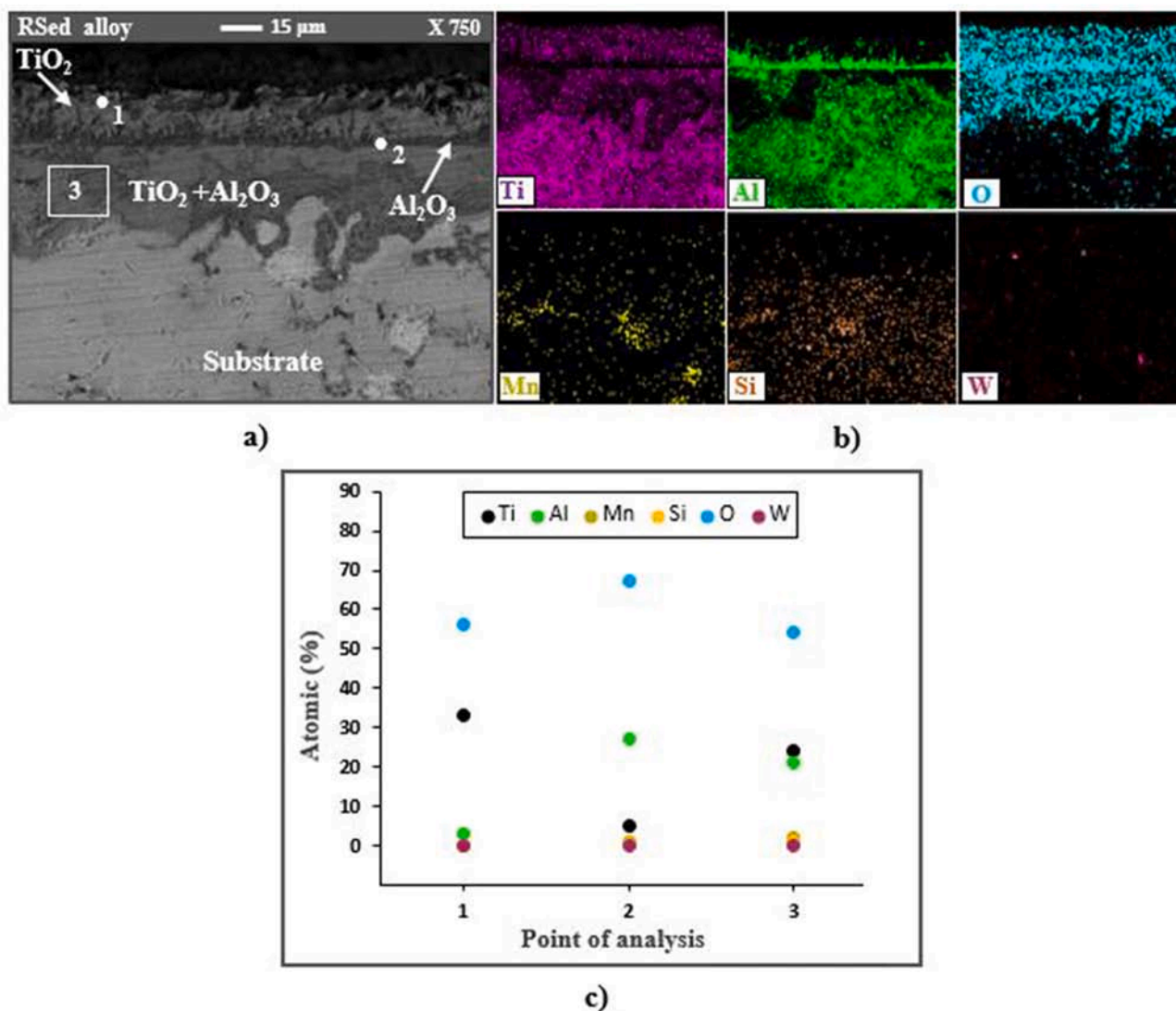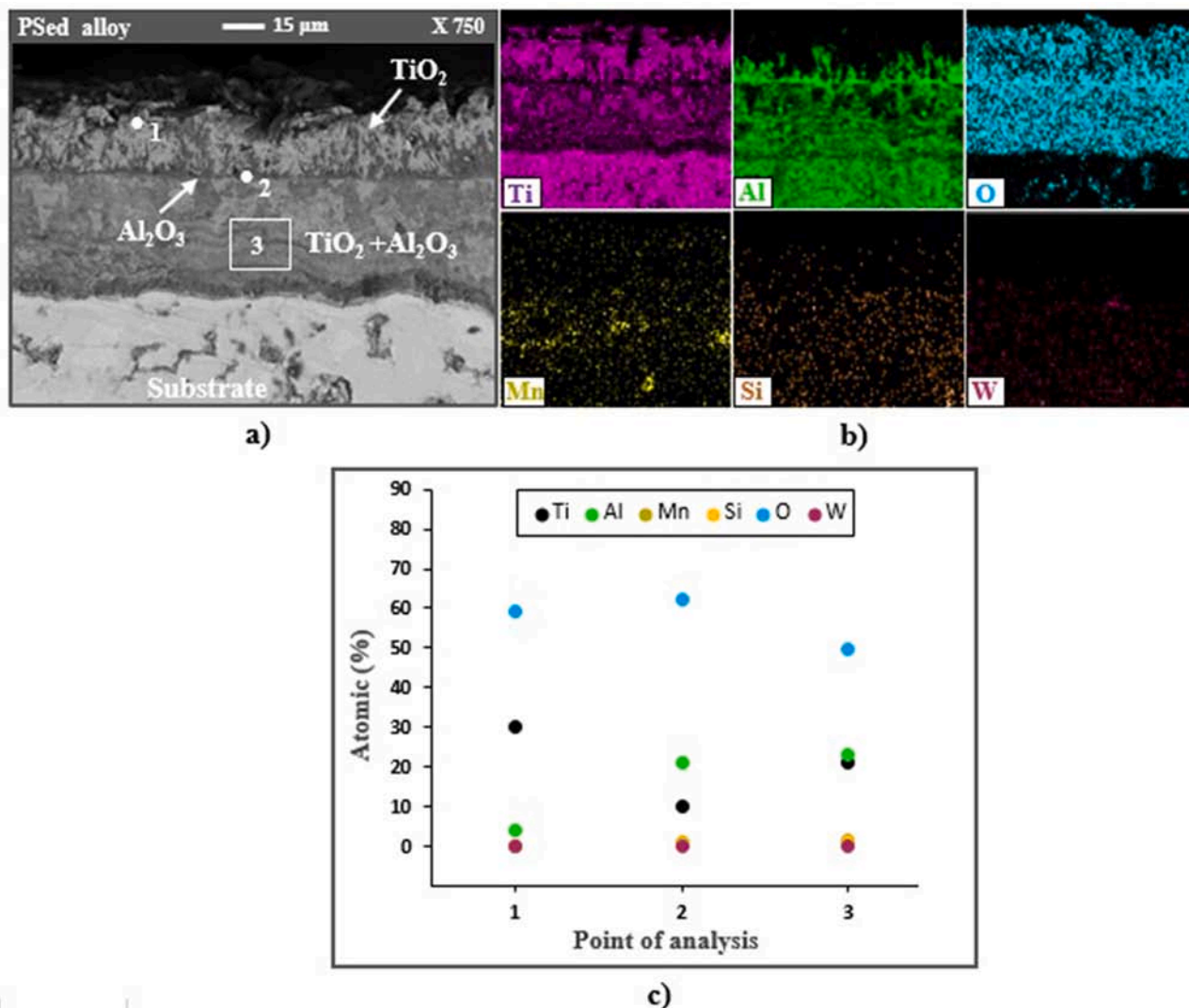
Fig. 12. PSed alloy after oxidation at 900 °C for 200 h: a) cross-sectional micrograph, b) EDS point analysis and c) EDS elemental mapping analysis.
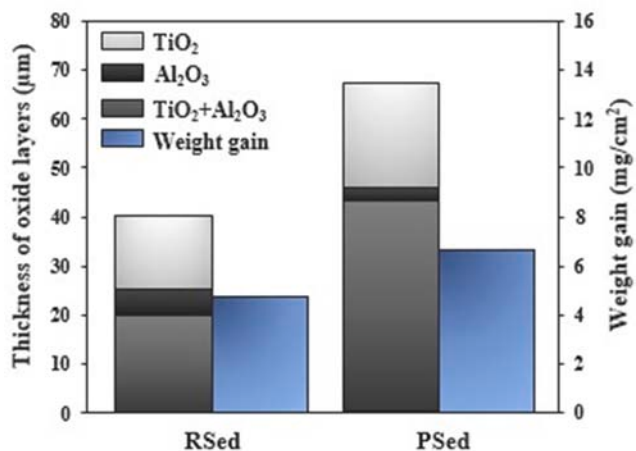
Fig. 13. The thickness of the oxide layers in the scale formed on both alloys after oxidation at 900 °C for 200 h.

adequately provided [35]. However, two kinetic factors are of great consideration in forming the outmost layer of the oxide scale. The first one is related to the fact that the diffusivity of Ti and Al in the phases building the alloy; the kinetic studies at 900 °C show that the diffusivity of Al in the γ and the α_2 phases is 2.41×10^{-18} and 6.82×10^{-19} while that of Ti in the γ and the α_2 phases is 1.06×10^{-17} and 3.18×10^{-18}, respectively [29]. As can be noticed, there is about an order of magnitude difference between the diffusivity of Al and Ti in the γ and α_2 phases. The latter factor can be explained based on the growth velocity of TiO_2 and Al_2O_3. The growth velocity of Al_2O_3 is much lower compared to TiO_2 as the activation energy of Al_2O_3 formation is much higher than that of TiO_2 formation [26]. These considerations allow us to conclude that the outmost layer of the oxide scale of investigated alloys will be formed by TiO_2 which is a fast-growing oxide, as evidenced in Figs. 11a and 12a (marked with 1). Furthermore, the formation of bumpy surface morphology is due to the much higher growth velocity of TiO_2 relative to Al_2O_3, as shown in Fig. 9a–c. The TiO_2 generated on the TiAl surface is characterized as polyporous and non-stoichiometry n-type oxide. It involves oxygen vacancies which provide the fast diffusion channel for oxygen, resulting in the higher oxidation rate [6,27], which is the reason why TiAl alloys exhibit weak oxidation resistance at elevated temperatures. As the oxidation continuous, the intermediate Al_2O_3 layer is created beneath the outmost TiO_2 layer as a result of the depletion of Ti. This Al_2O_3 layer plays an important role in preventing the further penetration of oxygen into the substrate, resulting in enhanced oxidation resistance [6]. Though the formation of Al_2O_3 on both scales is pronounced, the extent of formation

of this layer on the RSed alloy is higher in comparison with the PSed alloy, which is evident from the cross-section micrographs and elemental mapping analyses in Figs. 11 and 12. At 900 °C, the diffusivity of oxygen in TiO_2 is about four orders of magnitude higher than that in Al_2O_3 [29]. Therefore, the Al_2O_3 layer formed in the scale of RSed alloy is believed to retard the diffusion of O and Ti because it has thicker and more compact relative to formed that in PSed alloy. This fact highlights that the extent of formation of the TiO_2/Al_2O_3 mixed layer adjacent to the Al_2O_3 layer results in favor of the RSed alloy, as proved in Figs. 11a and 12a by cross-section micrographs of the alloys. However, despite the intermediate layer is constituted of the Al_2O_3, yet it could not inhibit the unfavorable inward diffusion of O. This observation can be related to the high growth velocity of TiO_2 which impairs the continuity of the Al_2O_3 layer. As a result of this fact, the hetero-phase mixture of $TiO_2+Al_2O_3$ continued to be formed by the interaction of outward diffusion of Ti/Al with inward diffusion of O during the oxidation experiment. Consequently, the cross-section micrographs show that the mixed layer of both alloys occupied the largest oxide scale volume. However, it is worth noting that the Al content has a strong relationship with the oxide scale structure of TiAl alloy. It was stated that the Al_2O_3 layer can be created on the outmost of TiAl alloys when the Al content reaches 60–70 at. % in air [36].

As pointed out before, the investigated alloys obey a nearly parabolic kinetic pattern because their power exponent is close to 2, indicating that the growth of both oxide scales was governed by diffusion processes. Analysis of the oxide growth on both scales indicates that the oxide scale mainly grows by inward transport of oxygen, as highlighted by many authors [28,30,34]. Therefore, it can be considered that the scale/substrate interface is moving towards the substrate because of the inward growing nature of the mixture of $TiO_2+Al_2O_3$ layer (Figs. 11a and 12a). During the isothermal oxidation experiments, the above-stated diffusion processes continue and causing the evolution of the multilayer scale structure, which is characteristic for TiAl alloys, that is to say, the oxide scale structures formed on both alloys are found to be in the order of inner mixture of $TiO_2+Al_2O_3$ layer, transient Al_2O_3 layer and outmost TiO_2 layer from the substrate/scale interface towards the surface.

The obtained results suggest that the processing route is a substantial factor when considering the oxidation behavior of alloys. A schematic diagram of the effect of the processing route on the scale structure formed on investigated alloys is depicted in Fig. 14. After oxidation at 900 °C for 200 h, the oxidation performance of RSed alloy is better than that of PSed alloy. The intrinsic defects caused during the sintering process behave as a short-diffusion path for the diffusion of species involved in the oxidation process, leading to the faster growth of oxide formed on the PSed alloy. Moreover, the Al_2O_3 discontinuities in the intermediate layer lead to increasing the outward diffusion of Ti, thereby facilitating the formation of outmost TiO_2 layer. Therefore, the thickness of the individual layers as well as that of the total scale increased as seen from the oxide scale of PSed alloy. In contrast, the reduction of inward oxygen transport contributed to enhancing the oxidation resistance of RSed alloy.

Some of the alloying elements that have attracted great attention in enhancing the oxidation resistance of TiAl alloys are W and Si [37,38]. But how the mechanism of oxidation is being affected by the alloying elements? The efficacy of Si in increasing the oxidation performance of TiAl can be described by the fact that it reduces the activity of Ti^{4+} ions by promoting the outward diffusion of Al to form an Al_2O_3 layer. This suppresses the formation and growth of TiO_2 layer [39]. However, the considerable Si content is required to provoke the creation of a protective Al_2O_3 layer [40]. With regard to the role of W addition, many researchers are in agreement [31,37,40] that the W is a beneficial addition element in enhancing the oxidation behavior of TiAl alloys. This beneficial role in terms of oxidation behavior is ascribed to the doping effect theory. That is to say, the addition of an alloying element with higher valance electron than that of Ti results in the decrease of defect

Fig. 14. Schematic diagram of the oxide scale structure formed on RSed (a), PSed (b) alloys after isothermal oxidation at 900 °C for 200 h and (c) the annihilation of oxygen ion vacancies in TiO_2 by doping W^{6+}.

concentration (or oxygen vacancy concentration) due to the maintaining electroneutrality condition in TiO_2 [36,41], as depicted in Fig. 14c. Consequently, the TiO_2 formation will be blocked in the oxide scale. This theory accounts for the decrease in the oxidation rate of W-containing TiAl alloys because the W has a higher valance electron than that of Ti. Moreover, a work done by Ping et al. [42] suggested the oxidation resistance of TiAl alloys correlates directly to the phase stability of the formed TiO_2 and Al_2O_3 oxides and formation energy of oxygen vacancy. They stated that the addition of alloying elements with d2 to d5 electrons such as W, Ta, Nb, Mo, Zr and Hf, reduces the stability of Al_2O_3 relative to that of TiO_2 and increases the formation energy of oxygen vacancy in TiO_2, thereby improving the oxidation resistance of TiAl alloys.

In a more recent investigation on the oxidation resistance of a spark plasma sintered Ti–48Al–2W-0.1B alloy at 800 °C, Bacos et al. [43] concluded that the enhanced oxidation resistance of the alloy stems from the doping effect due to the reduced velocity of diffusion in the W-doped TiO_2. Nevertheless, the beneficial effect of W in increasing the oxidation resistance of TiAl is not always absolute. According to a work done by Kim et al. [44], the high content of W addition (2 at.%) caused the concentration of W-rich phases all over the substrate due to the outward-diffused W during oxidation. They reported that the W content in TiAl–3Nb-0.3Si–2W alloy needs to be restricted below 2 at.% to eliminate the instability of microstructure in the substrate. Such W-rich phases were not observed in the substrate of RSed and PSed alloys, which is most likely due to the low contents of W in the alloy. This may be evidenced by the higher contents of W addition. As for the effect of Mn addition on the oxidation behavior of alloys, Mn ions with the valence of +2 or +3 are considered to have an adverse effect on the oxidation resistance of TiAl alloys due to the harmful doping effect [40]. In the case of alloying of the Mn to the TiAl, the doping effect renders the outmost TiO_2 layer overgrow, hence the oxidation resistance is significantly decreased. This phenomenon is in good agreement with the results reported by the Refs. [6,45,46]. The best consideration of Mn addition is to improve the room-temperature ductility [47] and sintering

characteristics [48] of TiAl alloys. In addition, a representative example of the progress in the practical application is the engine valve made out of TiAl-2.3Mn alloy developed by the Sumitomo Light Metal Industries [49].

4. Conclusions

The resistance sintering (RS) and pressureless sintering (PS) processing routes were effectively applied in the production of TiAl alloys having the composition Ti–44Al–2Si-1.7Mn-0.3W (at%). The alloys were isothermally oxidized at 900 °C for 200 h in order to determine the effect of processing route on the isothermal oxidation performance of the alloys. The results of this work suggest that processing routes play a major role in the oxidation performance of TiAl. The following main conclusions can be drawn from this work:

1. The duration of sintering process was 15 and 120 min for RS and PS methods. The rapid densification in the RS technology is due to the high heating rate and mechanical pressure.
2. The diffusion of the elements was completed for both alloys. However, only one region had pure W particles in RSed microstructure. In the case of PSed microstructure, there were few regions with a higher composition in W content.
3. Irrespective of whether the processing is performed via RS or PS, the microstructures of both alloys consisted of γ-TiAl and α_2-Ti$_3$Al phases. The relative density of RSed alloy (97.85%) was higher than that of the PSed alloy (92.32%). The microhardness of RSed alloy was somewhat higher.
4. After oxidation at 900 °C for 200 h, the final weight change of RSed alloy was 6.36 mg/cm^2 while that of PSed alloy was 8.92 mg/cm^2. Both alloys show a nearly parabolic oxidation response ($n \approx 2$). The oxidation rate constant of PSed alloy was 0.6391 mg^n cm^{-2n} h^{-1}, it is about 1.8 times higher than that of the RSed alloy. However, despite the lower content of Al, it should be said that the alloys exhibited good oxidation resistance compared to binary TiAl alloy (Ti–48Al) in our previous work because Si and W additions played an effective role in decreasing the oxidation rate of the alloys.
5. The formed oxidation products on the alloys are made up of TiO$_2$ and Al$_2$O$_3$ oxides. The oxide scale of both alloys is multilayered structure. The oxide scale structure is identified to be in the order of the inner mixture of TiO$_2$+Al$_2$O$_3$ layer, intermediate Al$_2$O$_3$ layer, and the outmost TiO$_2$ layer from the substrate/scale interface towards the surface. Moreover, both oxide scales have a good adherent relationship with the substrate. The thicker of the Al$_2$O$_3$ intermediate layer on the scale of RSed alloy is noteworthy. This layer reduces the velocity of O and Ti diffusion, and thus the thickness of oxide scale formed on the RSed alloy was decreased.
6. Although key factors are hard to identify, the enhanced oxidation performance of RSed alloy lies in the fact that the alloy has minimal porosity. This effect is considered to increase the oxidation performance of the alloy.

Author statement

Yigit Garip: Conceptualization, Experiment, Original draft preparation Writing- Reviewing and Editing.

Declaration of competing interest

The authors declare that they have no known competing financial interests or personal relationships that could have appeared to influence the work reported in this paper.

Appendix A. Supplementary data

Supplementary data to this article can be found online at https://doi. org/10.1016/j.intermet.2020.106985.

References

[1] O.F. Ogunbiyi, T. Jamiru1, E.R. Sadiku, L.W. Beneke, O.T. Adesina, T.A. Adegbola, Microstructural characteristics and thermophysical properties of spark plasma sintered Inconel 738LC, Int. J. Adv. Manuf. Technol. 104 (2019) 1425–1436, https://doi.org/10.1007/s00170-019-03983-w.

[2] W. Gui, J. Lin, M. Liu, Y. Qu, Y. Wang, Y. Liang, Effects of nano-NiO addition on the microstructure and corrosion properties of high Nb-TiAl alloy, J. Alloys Compd. 782 (2019) 973–980, https://doi.org/10.1016/j.jallcom.2018.12.200.

[3] R. Orru, R. Licheri, A.M. Locci, A. Cincotti, G. Cao, Consolidation/synthesis of materials by electric current activated/assisted sintering, Mater. Sci. Eng. R R 63 (2009) 127–287. https://doi.org/10.1016/j.mser.2008.09.003.

[4] T. Yener, A. Erdoğan, M.S. Gök, S. Zeytin, Nb and B effect on mechanical properties of Ti-Al based intermetallic materials, Vacuum 169 (2019) 1–9, https://doi.org/10.1016/j.vacuum.2019.108867.

[5] Y. Garip, O. Ozdemir, Comparative study of the oxidation and hot corrosion behaviors of TiAl-Cr intermetallic alloy produced by electric current activated sintering, J. Alloys Compd. 780 (2019) 364–377, https://doi.org/10.1016/j.jallcom.2018.11.324.

[6] Y. Garip, O. Ozdemir, A study of the cycle oxidation behavior of the Cr/Mn/Mo alloyed Ti-48Al-based intermetallics prepared by ECAS, J. Alloys Compd. 818 (2020) 1–14, https://doi.org/10.1016/j.jallcom.2019.152818.

[7] R.K. Gupta, B. Pant, P.P. Sinha, Theory and practice of $\gamma + \alpha_2$ Ti aluminide: a review, Trans. Indian Inst. Met. 67 (2) (2014) 143–165, https://doi.org/10.1007/s12666-013-0334-y.

[8] G.V. Krishna Pradeep, M. Duraiselvam, K.S. Prasad, A. Mohammad, Tribological behavior of additive manufactured γ-TiAl by electron beam melting, Trans. Indian Inst. Met. (2020), https://doi.org/10.1007/s12666-020-01950-8.

[9] G.S. Sankar, G.M. Karthik, A. Mohammad, R. Kumar, G.D. Janaki Ram, Friction welding of electron beam melted γ-TiAl alloy Ti-48Al-2Cr-2Nb, Trans. Indian Inst. Met. 72 (1) (2019) 35–46, https://doi.org/10.1007/s12666-018-1458-x.

[10] L. Wu, J. Wu, W. Wu, F. Cao, M. Jiang, Sol–gel-based coatings for oxidation protection of TiAl alloys, J. Mater. Sci. 55 (2020) 6330–6351, https://doi.org/10.1007/s10853-020-04466-0.

[11] D.J. Kim, D.Y. Seo, H. Saari, T. Sawatzky, Y.-W. Kim, Isothermal oxidation behavior of powder metallurgy beta gamma TiAl-2Nb-2Mo alloy, Intermetallics 19 (2011) 1509–1516. https://doi.org/10.1016/j.intermet.2011.05.027.

[12] J. Małecka, W. Grzesik, A. Hernas, An investigation on oxidation wear mechanisms of Ti-46Al-7Nb-0.7Cr-0.1Si-0.2Ni intermetallic-based alloys, Corrosion Sci. 52 (2010) 263–272. https://doi:10.1016/j.corsci.2009.09.015.

[13] K. Kothari, R. Radhakrishnan, N.M. Wereley, Advances in gamma titanium aluminides and their manufacturing techniques, Prog. Aero. Sci. 55 (2012) 1–16, https://doi.org/10.1016/j.paerosci.2012.04.001.

[14] M. Bik, A. Gil, M. Stygar, J. Dąbrowa, P. Jeleń, E. Długoń, M. Leśniak, M. Sitarz, Studies on the oxidation resistance of SiOC glasses coated TiAl alloy, Intermetallics 105 (2019) 29–38, https://doi.org/10.1016/j.intermet.2018.09.014.

[15] J. Sienkiewicz, S. Kuroda, R.M. Molak, H. Murakami, H. Araki, S. Takamori, K.J. Kurzyd1owski, Fabrication of TiAl intermetallic phases by heat treatment of warm sprayed metal precursors, Intermetallics 49 (2014) 57–64, https://doi.org/10.1016/j.intermet.2013.12.011.

[16] C.-L. Zhang, X.-J. Wang, X.-M. Wang, X.-S. Hu, K. Wu, Fabrication, microstructure and mechanical properties of Mg matrix composites reinforced by high volume fraction of sphere TC4 particles, J Magnes Alloy 4 (2016) 286–294, https://doi.org/10.1016/j.jma.2016.10.003.

[17] Y. Sun, J. Haley, K. Kulkarni, M. Aindow, E.J. Lavernia, Influence of electric current on microstructure evolution in Ti/Al and Ti/TiAl 3 during spark plasmasintering, J. Alloys Compd. 648 (2015) 1097–1103, https://doi.org/10.1016/j.jallcom.2015.07.079.

[18] U. Anselmi-Tamburini, J.E. Garay, Z.A. Munir, Fundamental investigations on the spark plasma sintering/synthesis process III. Current effect on reactivity, Mater. Sci. Eng., A 407 (2005) 24–30, https://doi.org/10.1016/j.msea.2005.06.066.

[19] G. Bernard-Granger, A. Addad, G. Fantozzi, G. Bonnefont, C. Guizard, D. Vernat, Spark plasma sintering of a commercially available granulated zirconia powder: comparison with hot-pressing, Acta Mater. 58 (2010) 3390–3399, https://doi.org/10.1016/j.actamat.2010.02.013.

[20] Z. Trzaska, G. Bonnefont, G. Fantozzi, J.-P. Monchoux, Comparison of densification kinetics of a TiAl powder by spark plasma sintering and hot pressing, Acta Mater. 135 (2017) 1–13, https://doi.org/10.1016/j.actamat.2017.06.004.

[21] J.E. Garay, S.C. Glade, U. Anselmi-Tamburini, P. Asoka-Kumar, Z.A. Munir, Electric current enhanced defect mobility in Ni$_3$Ti intermetallics, Appl. Phys. Lett. 58 (4) (2004), https://doi.org/10.1063/1.1774268.

[22] Z.A. Munir, U. Anselmi-Tamburini, M. Ohyanagı, The effect of electric field and pressure on the synthesis and consolidation of materials: a review of the spark plasma sintering method, J. Mater. Sci. 141 (2006) 763–777, https://doi.org/10.1007/s10853-006-6555-2.

[23] J. Xua, J. Lang, D. Ana, J. Liua, Z. Hua, Z. Xie, A novel alternating current-assisted sintering method for rapid densification of Al$_2$O$_3$ ceramics with ultrahigh flexural strength, Ceram. Int. 46 (2020) 5484–5488, https://doi.org/10.1016/j.ceramint.2019.10.287.

[24] M.A. Lagos, I. Agote, SPS synthesis and consolidation of TiAl alloys from elemental powders: microstructure evolution, Intermetallics 36 (2013) 51–56, https://doi.org/10.1016/j.intermet.2013.01.006.

[25] J.O. Abe, A.P.I. Popoola, O.M. Popoola, Consolidation of Ti6Al4V alloy and refractory nitride nanoparticles by spark plasma sintering method: microstructure, mechanical, corrosion and oxidation characteristics, Mater. Sci. Eng., A 774 (2020) 138920, https://doi.org/10.1016/j.msea.2020.138920.

[26] J. Dai, J. Zhu, C. Chen, F. Weng, High temperature oxidation behavior and research status of modifications on improving high temperature oxidation resistance of titanium alloys and titanium aluminides: a review, J. Alloys Compd. 685 (2016) 784–798, https://doi.org/10.1016/j.jallcom.2016.06.212.

[27] X. Gong, R.R. Chen, H.Z. Fang, H.S. Ding, J.J. Guo, Y.Q. Su, H.Z. Fu, Synergistic effect of B and Y on the isothermal oxidation behavior of TiAlNb-Cr-V alloy, Corrosion Sci. 131 (2018) 376–385, https://doi.org/10.1016/j.corsci.2017.12.013.

[28] D. Pilone, F. Felli, Isothermal oxidation behaviour of TiAl-Cr-Nb-B alloys produced by induction melting, Intermetallics 26 (2012) 36–39, https://doi.org/10.1016/j.intermet.2012.03.008.

[29] N.S. Neelam, S. Banumathy, A. Bhattacharjee, G.V.S. Nageswara Rao, Md Alam Zafir, Comparison of the isothermal and cyclic oxidation behavior of Cr and Mo containing γ-TiAlNb alloys, Corrosion Sci. 163 (2020) 108300, https://doi.org/10.1016/j.corsci.2019.108300.

[30] R. Swadźba, K. Marugi, Ł. Pyclik, STEM investigations of γ-TiAl produced by additive manufacturing after isothermal oxidation, Corrosion Sci. 169 (2020) 108617, https://doi.org/10.1016/j.corsci.2020.108617.

[31] P. Zhao, X. Li, H. Tang, Y. Ma, B. Chen, W. Xing, K. Liu, J. Yu, Improved high-temperature oxidation properties for Mn-containing beta-gamma TiAl with W addition, Oxid. Metals 93 (2020) 433–448, https://doi.org/10.1007/s11085-020-09964-9.

[32] V. Maurice, G. Despert, S. Zanna, P. Josso, M.-P. Bacos, P. Marcus, XPS study of the initial stages of oxidation of α₂-Ti₃Al and γ-TiAl intermetallic alloys, Acta Mater. 55 (2007) 3315–3325, https://doi.org/10.1016/j.actamat.2007.01.030.

[33] M.C. Galetz, A.S. Ulrich, C. Oskay, D. Fahsing, N. Laska, U. Schulz, M. Schütze, Oxidation-induced microstructural changes of the TiAl TNM-B1 alloy after exposure at 900 °C in air, Intermetallics 123 (2020) 106830, https://doi.org/10.1016/j.intermet.2020.106830.

[34] P.V. Cobbinah, W.R. Matizamhuka, Solid-state processing route, mechanical behaviour, and oxidation resistance of TiAl alloys, Ann. Mater. Sci. Eng. (2019) 1–21, https://doi.org/10.1155/2019/4251953.

[35] S.J. Qu, S.Q. Tang, A.H. Feng, C. Feng, J. Shen, D.L. Chen, Microstructural evolution and high-temperature oxidation mechanisms of a titanium aluminide based alloy, Acta Mater. 148 (2018) 300–310, https://doi.org/10.1016/j.actamat.2018.02.013.

[36] M. Naveed, A.F. Renteria, S. Weiß, Role of alloying elements during thermocyclic oxidation of β/γ-TiAl alloys at high temperatures, J. Alloys Compd. 691 (2017) 489–497, https://doi.org/10.1016/j.jallcom.2016.08.259.

[37] Y. Shida, H. Anada, Role of W, Mo, Nb and Si on oxidation of TiAl in air at high temperatures, Mater. Trans., JIM 35 (9) (1994) 623–631, https://doi.org/10.2320/matertrans1989.35.623.

[38] J. Małecka, W. Grzesik, A. Hernas, An investigation on oxidation wear mechanisms of Ti-46Al-7Nb-0.7Cr-0.1Si-0.2Ni intermetallic-based alloys, Corrosion Sci. 52 (2010) 263–272, https://doi.org/10.1016/j.corsci.2009.09.015.

[39] H.-R. Jiang, Z.-L. Wang, W.-S. Ma, X.-R. Feng, Z.-Q. Dong, L. Zhang, Y. Liu, Effects of Nb and Si on high temperature oxidation of TiAl, Trans. Nonferrous Metals Soc. China 18 (2008) 512–517, https://doi.org/10.1016/S1003-6326(08)60090-4.

[40] D.-B. Lee, Effect of Cr, Nb, Mn, V, W and Si on high temperature oxidation of TiAl alloys, Met. Mater. Int. 11 (2) (2005) 141–147, https://doi.org/10.1007/BF03027458.

[41] D. Vojtech, T. Popela, J. Kubásek, J. Maixner, P. Novák, Comparison of Nb- and Ta-effectiveness for improvement of the cyclic oxidation resistance of TiAl-based intermetallics, Intermetallics 19 (2011) 493–501, https://doi.org/10.1016/j.intermet.2010.11.025.

[42] F.P. Ping, Q.M. Hu, A.V. Bakulin, S.E. Kulkova, R. Yang, Alloying effects on properties of Al₂O₃ and TiO₂ in connection with oxidation resistance of TiAl, Intermetallics 68 (2016) 57–62, https://doi.org/10.1016/j.intermet.2015.09.005.

[43] M.-P. Bacos, S. Ceccacci, J.-P. Monchoux, C. Davoine, T. Gheno, C. Rio, A. Morel, J.-S. Merot, F. Fossard, M. Thomas, Oxidation behavior of a spark plasma sintered Ti-48Al-2W-0.1B alloy at 800°C, Oxid. Metals 93 (2020) 587–600, https://doi.org/10.1007/s11085-020-09973-8.

[44] D. Kim, D. Seo, S.-W. Kim, S.-E. Kim, D.-Y. Keum, J.-K. Hong, Cyclic oxidation behaviors of TiAl-Nb-Si-based alloys, Oxid. Metals 86 (2016) 417–430, https://doi.org/10.1007/s11085-016-9644-x.

[45] S.A. Kekare, P.B. Aswath, Oxidation of TiAl based intermetallics, J. Mater. Sci. 32 (1997) 2485–2499, https://doi.org/10.1023/A:1018529829167.

[46] Y. Shida, H. Anada, The effect of various ternary additives on the oxidation behavior of TiA1 in high-temperature air, Oxid. Metals 45 (1996) 197–219, https://doi.org/10.1007/BF01046826.

[47] N. Cui, F. Kong, X. Wang, Y. Chen, H. Zhou, Microstructural evolution, hot workability, and mechanical properties of Ti-43Al-2Cr-2Mn-0.2Y alloy, Mater. Des. 89 (2016) 1020–1027, https://doi.org/10.1016/j.matdes.2015.10.076.

[48] M. Kumagai, K. Shibue, M.-S. Kim, M. Yonemitsu, Influence of chlorine on the oxidation behavior of TiAl-Mn intermetallic compound, Intermetallics 4 (1996) 551–566, https://doi.org/10.1016/0966-9795(96)00043-X.

[49] S. Taniguchi, T. Shibata, Influence of additional elements on the oxidation behaviour of TiAl, Intermetallics (1996) 585–593, https://doi.org/10.1016/0966-9795(96)00017-9.